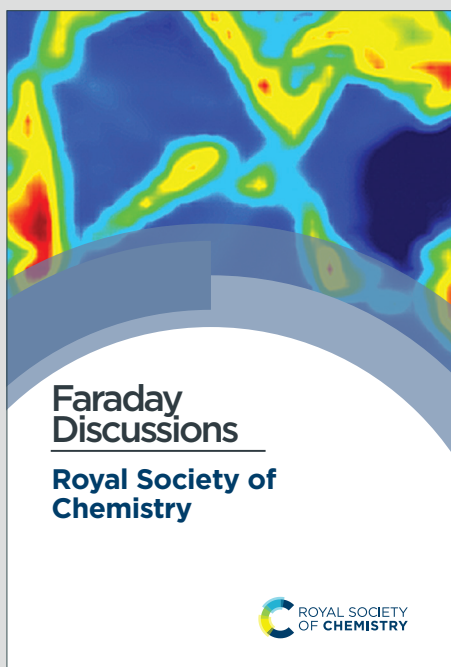


Faraday Discussions

Accepted Manuscript



This is an Accepted Manuscript, which has been through the Royal Society of Chemistry peer review process and has been accepted for publication.

Accepted Manuscripts are published online shortly after acceptance, before technical editing, formatting and proof reading. Using this free service, authors can make their results available to the community, in citable form, before we publish the edited article. We will replace this Accepted Manuscript with the edited and formatted Advance Article as soon as it is available.

You can find more information about Accepted Manuscripts in the [Information for Authors](#).

Please note that technical editing may introduce minor changes to the text and/or graphics, which may alter content. The journal's standard [Terms & Conditions](#) and the [Ethical guidelines](#) still apply. In no event shall the Royal Society of Chemistry be held responsible for any errors or omissions in this Accepted Manuscript or any consequences arising from the use of any information it contains.

This article can be cited before page numbers have been issued, to do this please use: G. Rajaraman and A. Sen, *Faraday Discuss.*, 2021, DOI: 10.1039/D1FD00072A.

Can you Break the Oxo-Wall? – A Multiconfigurational Perspective

View Article Online

DOI: 10.1039/D1FD00072A

Asmita Sen and Gopalan Rajaraman*

Department of Chemistry, Indian Institute of Technology Bombay, Mumbai-400076, India.

E-mail: rajaraman@chem.iitb.ac.in

Abstract:

The concept of “OXO-WALL” was conceived about 60 years ago by Harry B. Gray, which is found to be related to the non-existence of high-valent M-Oxo species in +IV oxidation state in a tetragonal geometry beyond group 8 in the periodic table. Several efforts have been made in the past decades to test and find examples that violate this theory. Several claims of violation in the past were attributed to the difference in the geometries/coordination number and, therefore, these are not examples of true violation. In recent years, substantial efforts have been undertaken to synthesise a true $\text{Co}^{\text{IV}}=\text{O}$ species with various ligand architectures. The $\text{Co}^{\text{IV}}=\text{O}$ and $\text{Co}^{\text{III}}-\text{O}^\bullet$ are electromers, while interchangeably used in the literature; the former violates the oxo-wall while the latter does not. The possibility that these two species could exist in various proportions similar to resonating structures has not been considered in detail in this area. Further, there are no attempts to quantify such mixing. In this direction, we have employed the density function theory (DFT) and *ab initio* CASSCF/NEVPT2 method to quantify the co-existence of $\text{Co}^{\text{IV}}=\text{O}$ and $\text{Co}^{\text{III}}-\text{O}^\bullet$ isomeric species. By thoroughly studying six different metal-oxo species, we affirm that the nature of such electromeric mixing is minimal/negligible for $\text{Fe}^{\text{IV}}=\text{O}$ and $\text{Mn}^{\text{IV}}=\text{O}$ species – both are pre-oxo-wall examples. By studying four different ligand architecture with Co-oxo species, our results unveil that the mixing of the $\text{Co}^{\text{IV}}=\text{O} \leftrightarrow \text{Co}^{\text{III}}-\text{O}^\bullet$ is substantial in all geometries, with dominant $\text{Co}^{\text{IV}}=\text{O}$ species favourable for $S = 3/2$ intermediate spin state. The per cent of $\text{Co}^{\text{III}}-\text{O}^\bullet$ species enhances substantially for $S = 1/2$ low-spin state. We have attempted to develop a tool to estimate the per cent of $\text{Co}^{\text{III}}-\text{O}^\bullet$ species using various structural parameters. Among tested, a linear relationship between % $\text{Co}^{\text{III}}-\text{O}^\bullet$ and a bond length based ratio is found ($R_d = \frac{d_{(\text{Co}-\text{O})}}{d_{(\text{Co}-\text{N}_{\text{ax}})}}$ here $d_{(\text{Co}-\text{O})}$ and $d_{(\text{Co}-\text{N}_{\text{ax}})}$ are axial Co–O and Co–N_{ax} bond lengths in Å). It is found that the higher the R_d , the greater will be the $\text{Co}^{\text{III}}-\text{O}^\bullet$ character and the geometrically portable correlation developed offers a way to qualitatively compute % of $\text{Co}^{\text{III}}-\text{O}^\bullet$ character for unknown geometries.

Introduction:

The most important biological oxidative processes, water oxidation during photosynthesis in photosystem II and oxygen reduction in respiration, are found to be catalysed by multiply bonded high-valent terminal Mn/Fe-oxo species.^{1,2} Apart from these naturally occurring enzymatic reactions, high-valent terminal as well as bridging Fe/Mn-dependent synthetic models mimicking these metalloenzymes are proposed to be key intermediates in oxidative transformations of various organic molecules. In the past few decades, these active intermediates have been synthesised, spectroscopically characterised, and their mechanism in activating C-H/O-H/N-H bonds was explored.^{3 4 5 6 7 8 9} For instance, various biomimic high-valent Fe^{IV}=O dependent models of heme and non-heme metalloenzymes were found to play an active role in O₂ activation. Similarly, in photosystem II, a high-valent Mn-oxo species is found to catalyse the most important O–O bond formation step, although this species is elusive. However, a number of monomeric or dimeric high-valent biomimic Mn-oxo species were synthesised, characterised, and proven to be superior to Fe catalyst. Further, early transition metals such as Cr, V, and Mo have been investigated to understand the electronic effect on the catalytic transformations of several metalloenzymes and design a robust catalyst.¹⁰ Although the chemistry of first-row early transition metals with terminal oxo group is well-established, for the late transition metals such as Co, Ni, and Cu elements, a high oxidation state (+4) terminal oxo species are rare and are non-existent for a tetragonal geometry. An invisible wall, namely “OXO WALL”, is proposed to separate the Fe–Ru–Os and Co–Rh–Ir triads in the periodic table.^{11, 12, 13}

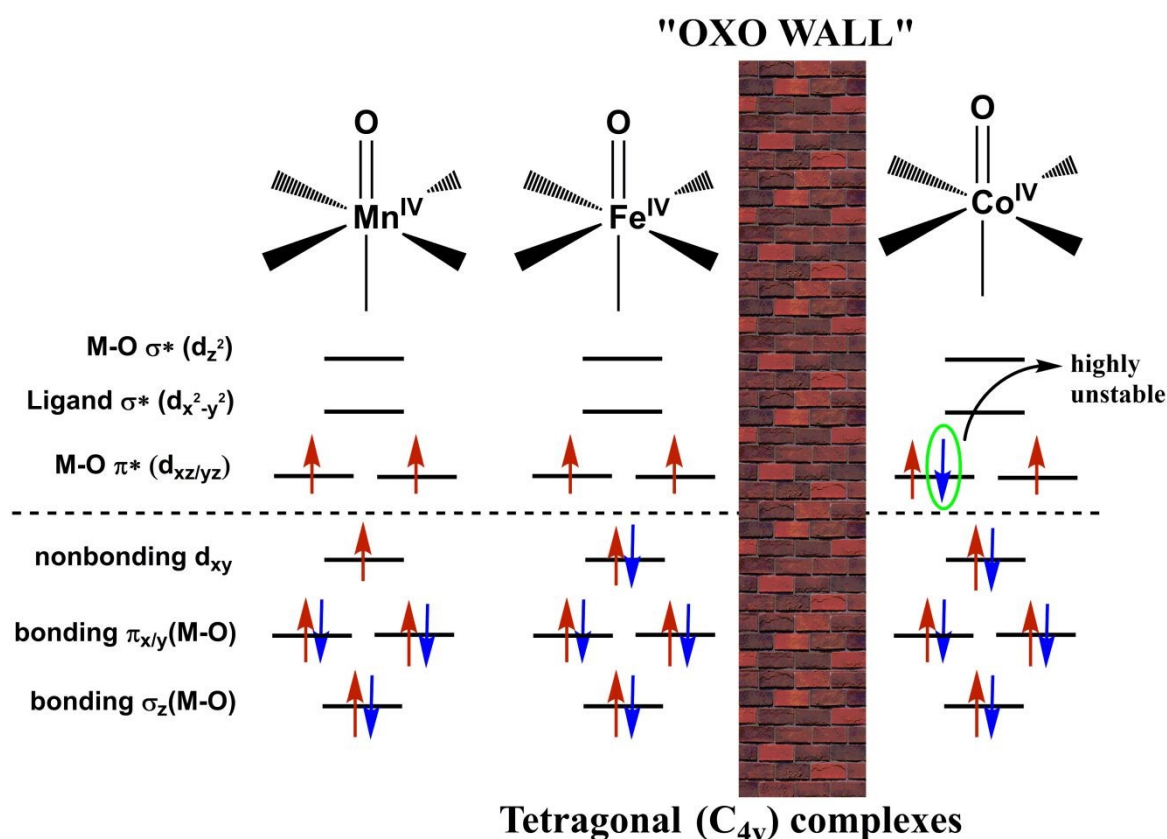
The story of “OXO WALL” was conceived about 60 years ago in Copenhagen by Harry B. Gray, who proposed the existence of V^{IV}-oxo triple bond (V≡O) for a d¹ vanadyl ion (VO²⁺) employing a modified molecular orbital diagram including oxo-metal π-bonding.^{14, 12, 11} Later, this triple bond (M≡O) formulation has been identified in d⁰, d¹, d² (low-spin) monomeric M-oxo tetragonal complexes including CrO³⁺, MoO³⁺ etc.^{15, 16} The modified molecular orbital diagram in these tetragonal terminal M-oxo species composed of a lowest-lying M–O σ-bonding orbital, followed by the degenerate M–O π-bonding orbitals, a nonbonding metal-d_{xy} orbital, two degenerate M–O π* antibonding orbitals (d_{xz/yz}), σ* antibonding d_{x²-y²} orbital and highest lying M–O σ* antibonding d_{z²} orbital [$\sigma_z(\text{M-O}) < \pi_x(\text{M-O}) = \pi_y(\text{M-O}) < \text{nb}(d_{xy}) < \pi_x^*(d_{xz}) = \pi_y^*(d_{yz}) < \sigma^*(d_{x^2-y^2}) < \sigma^*(d_{z^2})$, Scheme 1]. Apart from the M–O σ and π-bonding orbitals, for d⁰, d¹, d² (low-spin) systems, the first two d-electrons occupy the nonbonding d_{xy} orbital, yielding π bond-order of 2. This value decreases to 3/2, 1 and 1/2 if we move from d³ to d⁵ electronic configurations as the additional d-electrons in these configurations enter π* antibonding d_{xz} and d_{yz} orbitals. Thus enhancing the electron occupancy in π*-orbitals reduce the π bond order in tetragonal d⁵-M^{IV}=O complexes (Scheme 1). The d-orbital splitting pattern of C_{4v} symmetric L₅M(O) complexes with more than 5 electrons in the metal-d-orbitals lead to the M–O π-bond order of 0.5, making the oxo group extremely basic and undergo either protonation or dimerisation or attacked by electrophiles.¹⁶ To obtain high M–O π-bond multiplicity for elements beyond Fe, the oxidation state needs to be very large (≥ +5), making the complex unstable and susceptible to the elimination of O₂ or H₂O₂. As a summation of all these effects to limit the metal oxidation state as high as +4 and at the same time limit to a lower number of d-electrons, generates a wall between the groups 8 and 9 in the periodic table. On the left-hand side (V-Fe), the d⁴ electronic configuration leads to an oxidation state +4 or

View Article Online
DOI: 10.1039/C2FD00072A

lower, whereas on the right side of the periodic table formal oxidation state should be +5 or higher to form M–O multiple bonds.

View Article Online
DOI: 10.1039/D1FD00072A

There are many reports where the reactivity of $\text{Fe}^{\text{IV}}=\text{O}$ species was attributed to its valance isomer $\text{Fe}^{\text{III}}-\text{O}^\bullet$ (oxyl- Fe^{III} species), which gets stabilised upon the approach of electrophiles.¹⁷ For $\text{Mn}^{\text{IV}}=\text{O}$ species, on the other hand, a complex set of spin-state reactivity emerged where the role of $\text{Mn}^{\text{III}}-\text{O}^\bullet$ (oxyl- Mn^{III} species) in dictating the reactivity is ruled out.¹⁸ It is clear from these contrasting examples that understanding the nature of metal multiple bond oxo species is important to decipher its reactivity. Although adequate attention has been paid to the structural perspective of high-valent tetragonal (C_{4v}) Fe/Mn–O complexes with multiple bonds, there are only limited studies on species' stability and electronic structure on the other side of the wall. Particularly, several recent reports focus their attention on the formation of $\text{Co}^{\text{IV}}-\text{O}$ or its valance isomer $\text{Co}^{\text{III}}-\text{O}^\bullet$ species and very little is explored with respect to their structure and bonding and has high relevance to many catalytic processes, including water oxidation.¹⁹ The oxo-wall theory suggests that the formation of multiple bonds is unstable between Co and oxo moiety when Co-centre is in a +4 oxidation state (d^5 -system). There are efforts to seek violation of oxo-wall theory in this respect, and there are claims and counterclaims.¹⁹ As these species are extremely transient in nature, establishing structure and bonding is challenging, especially given that $\text{Co}^{\text{IV}}=\text{O}$ and its valance isomer $\text{Co}^{\text{III}}-\text{O}^\bullet$ can not be easily distinguished unless sophisticated experiments such as EPR/ENDOR experiments were carried out with labelled oxygen atoms.²⁰ Further, there are also attempts to stabilise formal $\text{Co}^{\text{IV}}=\text{O}$ species in other coordination environments, such as a trigonal planer, square pyramidal etc. Nam and Ray groups have photochemically synthesised a square pyramidal $[(13\text{-TMC})\text{Co}^{\text{IV}}(\text{O})]^{2+}$ complex



Scheme 1: Pictorial representation of the “OXO WALL” in tetragonal (C_{4v}) high-valent Fe/Mn/Co-oxo complexes.

that has been characterised as formal $\text{Co}^{\text{IV}}=\text{O}$ species. Further, it is hard to rule out the possibility of $\text{Co}^{\text{IV}}=\text{O}$ and its valence isomer $\text{Co}^{\text{III}}-\text{O}\cdot$ species co-existing in a mixed form with various proportions. Such a possibility challenges various experimental, spectral and analytic interpretations, which often assumes the existence of only one species in solution.

To understand the delicate balance between the two valence isomers $\text{Co}^{\text{IV}}=\text{O}$ and $\text{Co}^{\text{III}}-\text{O}\cdot$ species in relation to the oxo wall theory proposed by Gray, we have performed Density Functional Theory (DFT) and ab-initio CASSCF/NEVPT2 calculations on a series of tetragonal $\text{L}_5\text{M}(\text{O})$ high-valent Co-oxo complexes, namely, $[(15\text{-TMC})\text{Co}(\text{O})(\text{CH}_3\text{CN})]^{2+}$ (**1**), $[(13\text{-TMC})\text{Co}(\text{O})(\text{CH}_3\text{CN})]^{2+}$ (**2**), and $[(\text{N4Py})\text{Co}(\text{O})]^{2+}$ (**3**) complexes (where 15-TMC is 1,5,9,12-tetramethy-1,5,9,12-tetraazacyclotridodecane, 13-TMC is 1,4,7,10-tetramethy-1,4,7,10-tetraazacyclotridecane and N4Py is N,N-bis(2-pyridylmethyl)-N-bis(2-pyridyl)methylamine). Further, we have extended our studies to $[(13\text{-TMC})\text{Co}(\text{O})]^{2+}$ (**4**), $[(\text{N4Py})\text{Fe}(\text{O})]^{2+}$ (**5**) and $[(\text{N4Py})\text{Mn}(\text{O})]^{2+}$ (**6**) to thoroughly analyse and understand the existence of electromers $\text{M}^{\text{IV}}=\text{O}$ vs $\text{M}^{\text{III}}-\text{O}\cdot$ species in these complexes. Our study aims to answer the following questions (i) before and after the wall: Is there a $\text{M}^{\text{IV}}=\text{O} \leftrightarrow \text{M}^{\text{III}}-\text{O}\cdot$ equilibrium or co-existence of these species in proportions? (ii) does the individual spin state play a role in breaking the wall? (iii) does geometry/ligand architecture control the character of the $\text{Co}^{\text{IV}}=\text{O}/\text{Co}^{\text{III}}-\text{O}\cdot$ species? (iv) is a black-box tool to quantify $\text{Co}^{\text{III}}-\text{O}\cdot$ character for unknown structure possible?

Computational Details:

Density Functional Theory (DFT) calculation: The geometries of all complexes in the present study have been optimised employing Density Functional Theory (DFT) method using the Gaussian 16 suit of program²¹. An unrestricted dispersion-corrected B3LYP hybrid density functional²²⁻²³ (B3LYP-D3) along with a double- ξ quality LanL2DZ²⁴ with Los Alamos effective core potential basis set for the metal and 6-31G* formalism for the rest of the atoms (H, C, N, O)²⁵ have been used for the geometry optimisation as well as frequency calculations in the gas phase. The gas-phase energetics have been refined further by the single-point calculations using an all-electron def2-TZVP basis set in the same B3LYP-D3 level of theory. The solvation energies are integrated using the solvation model based on density (SMD) solvation model²⁶ in the acetone Solvent using the same methodology. The final energies are the B3LYP-D3 computed Gibbs free energy corrected solvation energies. The energy correction terms are obtained from the vibrational frequency calculations in the gas phase.

Ab initio calculations: All *ab initio* calculations have been carried out using the ORCA 4.2.1 program.²⁷ For these calculations, the scalar-relativistic effect has been incorporated using the Douglas–Kroll–Hess (DKH) Hamiltonian.²⁸ The starting guess orbitals were found performing ROKS calculations on the DFT optimised structures as well as several points obtained from the scanning along the M-O as well as M-N_{ax} bonds using BP86 functional, DKH-def2-TZVP basis set for the metal, DKH-def2-TZVP(-f) for the directly coordinated N, O atoms to metal and DKH-def2-SVP basis set for the rest of the atoms (C and H). For further CASSCF/NEVPT2 calculations similar basis set as ROKS has been used. For all calculations, an active space of CAS(n,8) has been employed using electrons in five metal-d-orbitals and three oxo p-orbitals including two oxo p_π (π_x and π_y) orbitals and one oxo p_σ (σ_z) orbital. For d^4 and d^5 metal centres, 5 quintet, 45 triplet, 50 singlet roots and one sextet, 24 quartets, 75 doublet roots were considered, respectively. By these calculations, the electronic wave-functions were

expanded in all possible configuration state functions by the distribution of a number of electrons in the total number of active spaces employing the complete active space self-consistent-field (CASSCF) method.

View Article Online
DOI: 10.1039/D1FD00072A

Results and Discussion:

Ab initio quantification of $\text{Co}^{\text{IV}}=\text{O}$ and $\text{Co}^{\text{III}}-\text{O}^{\cdot}$ electromerism:

In the following section, we have attempted to comprehend how the so-called oxo-wall operates in various high-valent octahedral (O_h) or pseudo octahedral M-oxo complexes beyond group 8 in the periodic table. To quantify the co-existence of isomeric $\text{Co}^{\text{IV}}=\text{O}$ and $\text{Co}^{\text{III}}-\text{O}^{\cdot}$

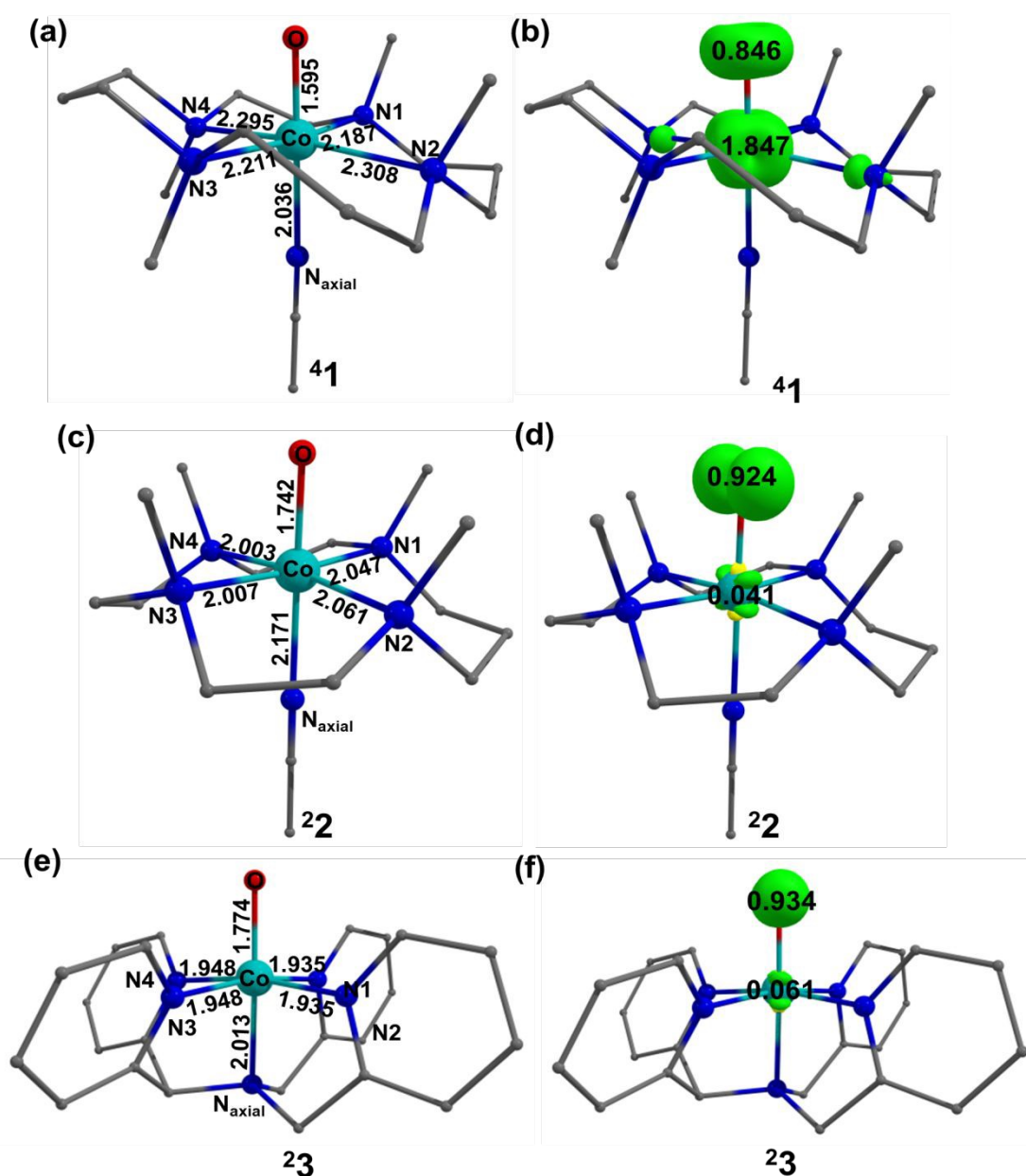


Figure 1: (a,c,e) B3LYP-D3 optimised structure and (b,d,f) spin density plots of the ground state of complexes 1-3.

form, we have chosen the complexes possessing an octahedral $[L_5M(O)]$ type of geometry with the Co centre in a high-oxidation state (+III or +IV). These contain either (i) a tetradentate ligand with two axial positions occupied by the oxo ligand and one relatively loosely bound N-donor ligand, such as, $[(15\text{-TMC})\text{Co}(\text{O})(\text{CH}_3\text{CN})]^{2+}$ (**1**), $[(13\text{-TMC})\text{Co}(\text{O})(\text{CH}_3\text{CN})]^{2+}$ (**2**) complexes (ii) or a pentacoordinate ligand where the axial position opposite to the oxo ligand is strongly bound to the metal, e.g. $[(\text{N4Py})\text{Co}(\text{O})]^{2+}$ (**3**) complex. All three complexes are found to have a pseudo- C_s symmetry (Chemcraft calculated $R = 0.661, 0.392, 0.000$, respectively).²⁹ The tetragonal C_{4v} symmetry has been lifted in complexes **1** and **2** by modification of the cyclam ligand (1,4,8,11-tetraazacyclotetradecane). In 15-TMC ligand architecture an extra methylene group is added, and in 13-TMC (1,4,7,10-tetramethyl-1,4,7,10-tetraazacyclotridecane) a methylene group is removed. The symmetry in complex **3** has been lifted due to the presence of a tertiary methyl group connected to the apical N-atom. Complex **3** has an ideal C_s symmetry while the other two deviates significantly.

Complex **1** is found to have an $S = 3/2$ intermediate state as the ground state, with the high-spin $S = 5/2$ and low-spin $S = 1/2$ states are lying at 64.0 kJ/mol and 13.7 kJ/mol, respectively. In contrast, for complexes **2** and **3**, an $S = 1/2$ low-spin state is the ground state. The energy gaps between the ground state and other states viz $S = 5/2$ and $3/2$ spin states for **2** are very small (7.8 kJ/mol and 22.9 kJ/mol, respectively,) while these spin-states lie comparatively higher in energy in complex **3** (99.9 kJ/mol and 32.1 kJ/mol, respectively). In the ground state optimised geometry, the respective Co–O and Co–N_{ax} bond distances are found to be 1.595 Å and 2.036 Å; 1.742 Å and 2.171 Å; and 1.770 Å and 2.013 Å respectively in **1-3**. The other four Co–N_{eq} (Co–N1, Co–N2, Co–N3 and Co–N4) bonds in **1-3** are 2.187 Å, 2.308 Å, 2.211 Å, 2.295 Å; 2.047 Å, 2.061 Å, 2.007 Å, 2.003 Å and 1.935 Å, 1.935 Å, 1.948 Å, 1.948 Å, respectively. The

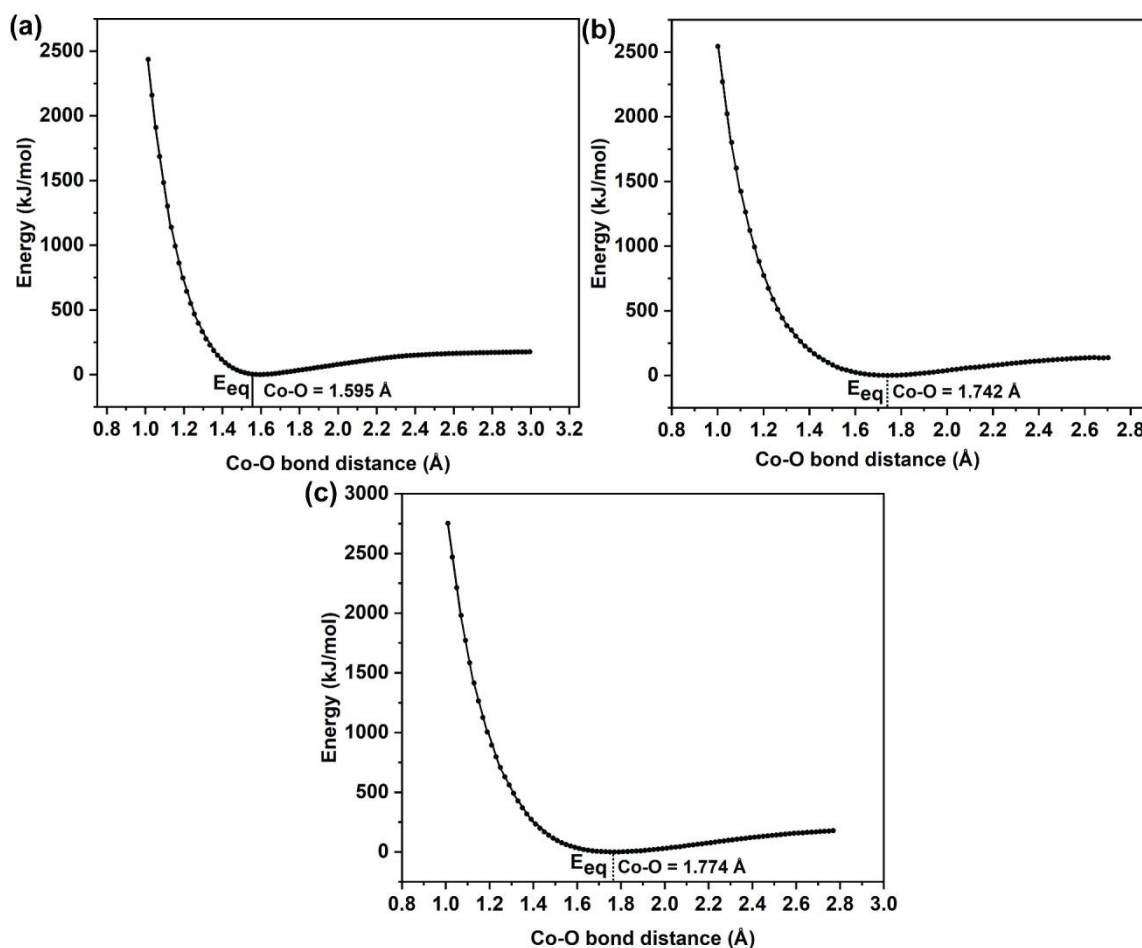


Figure 2: DFT estimated potential energy scan surfaces of the lowest-energy states of (a-c) **1-3** as a function of the Co–O distance.

bonding parameters point towards the higher symmetric geometry in complex **3** and a lower one in **1**.³⁰ Although experimental geometrical parameters are unavailable for complexes **1-3**, we compared the geometries with the structurally similar species reported. Particularly the geometry of complex **3** resembles another Co^{IV} species reported, and the Co–N_{avg} distanced reported for this species agrees with our calculated results.³¹ Further, the DFT computed Co–O bond stretching frequency values are calculated to be 886 cm⁻¹, 621 cm⁻¹ and 615 cm⁻¹ for **1-3**, respectively. The Co–O bond stretching frequency for a true Co^{IV}=O is reported to be 840 cm⁻¹.³² Benchmarking the above results with this value suggests that complex **1** is likely to be closer to an ideal Co^{IV}=O species while the values for species **2** and **3** are significantly deviating. This suggests a strong deviation for **2** and **3** from an ideal Co^{IV}=O form.

In complexes **1-3**, the DFT computed spin densities on (Co:O) pairs are (1.847: 0.846), (0.041: 0.924), and (0.061:0.934), respectively. The spin-up α -electron density of ~ 2 in **1** and ~ 0 in **2** and **3** on the metal indicates +III oxidation state on Co rather than a +IV oxidation state which always gives a residual spin value close to 5.0/3.0/1.0 depending on the nature of the spin states (high-spin, intermediate spin or low spin). Secondly, the DFT methodology employed tends to overestimate the delocalisation of spin densities resulting in larger than expected spin densities on the M=O oxyl O atom. This is one of the well-established limitations of DFT methods.³³

Apart from spin densities, the charges on the metal centre are also often underestimated by DFT methods, with the metallic centre exhibiting a significant loss of charge with a concomitant gain on the ligands.^{34, 35} Additionally, for Mn^{III/IV/V}=O species Borovik and co-workers have eliminated the possibility of Mn–O[•] character with the help of EPR spectroscopy, albeit DFT calculations seemingly indicate a strong radical character at the oxyl centre.³⁶ All these arguments suggest that DFT calculated spin densities to assess the true nature of Co^{IV}=O vs Co^{III}–O[•] species is not reliable. Further, the DFT methods are a single determinant approach, and chances of having a multiconfigurational character for the ground state within or among these two species cannot be accounted for by these methods. Further, when the metal-oxo bond is elongated far from the equilibrium geometry, this is likely to stabilise the high-spin state as the ground state with a significant radical character generated at the oxyl oxygen. Earlier method assessment of various functionals, including B3LYP against RCCSD(T) method, reveals that the structure and energetics match better between the two methods for the ground state geometries. However, for the excited state (in this case, S = 2 Fe^{IV}=O species), a larger deviation between B3LYP and ab initio RCCSD(T) was found.³⁷

As the radical character at the oxyl oxygen atom is crucial to prove/disprove the oxo wall theory, a robust method that does not suffer from the above limitations is required. Although several accurate wave-function (WF) based methods are available, many sophisticated methods are computationally expensive, limiting their usage on realistic molecules. For these reasons, we turn to CASSCF/NEVPT2 methods.^{38, 39} The CASSCF calculations are multiconfigurational self-consistent field methods, where the number of determinants is used for the expansion of the CI vector is defined by the division of the orbitals in subspaces. The orbitals and electrons are chosen, such as those that contribute most to explain the system. The total number of electrons are distributed equally among the active space, resulting in a non-integer number of electrons. The CASSCF/NEVPT2 method is also plagued by computational cost, reference space problems, issues with the dynamic correlation. Moreover, the optimised geometry is taken from the DFT method and, therefore, not a true minimum in these WF based methods. However, apart from these pros and cons, the *ab initio* CASSCF/NEVPT2 method is

believed to give a better description of the wave function of a system if apt reference space is chosen. Hence in this study, we have performed ab initio CASSCF/NEVPT2 calculations to assess and understand the existence of these two isomeric forms.

View Article Online
DOI: 10.1039/D1FD00072A

Our CASSCF/NEVPT2 results show that the DFT calculated ground states and energy ordering of the high-lying states in **I-3** agrees with each other, offering confidence in the results. Herein we have employed a CAS(11,8) active space including five metal-d orbitals and three oxo 2p orbitals (p_x , p_y and p_z) to understand the nature of the dominant electromeric form. The NEVPT2 calculated $S = 5/2$ and $S = 1/2$ states are lying at 117.8 kJ/mol and 93.0 kJ/mol; 126.0 kJ/mol and 55.2 kJ/mol; 167.0 kJ/mol and 99.4 kJ/mol respectively for complexes **I-3**.

At the equilibrium Co–O bond lengths of 1.595 Å for species **1** the state-average CAS(11,8) SCF calculation yield following electronic configuration $\sigma_{(pz+dz^2)}^2 \pi_{(py+dyz)}^2 \pi_{(px+dxz)}^2 \square_{(dxy)}^2 \pi_{(py+dyz)}^1 \pi_{(px+dxz)}^1 \square_{(dx^2-y^2)}^1 \sigma_{(pz+dz^2)}^0$. Here the p_x , p_y and p_z orbitals correspond to the oxyl oxygen atom. This electronic configuration corresponds to an ideal $\text{Co}^{\text{IV}}=\text{O}$ species, and this was found to contribute 77.5% to the ground state wavefunction. Additionally, $\sigma_{(pz+dz^2)}^1 \pi_{(py+dyz)}^2 \pi_{(px+dxz)}^2 \square_{(dxy)}^2 \pi_{(py+dyz)}^1 \pi_{(px+dxz)}^1 \square_{(dx^2-y^2)}^1 \sigma_{(pz+dz^2)}^1$ configuration that corresponds to $\text{Co}^{\text{III}}-\text{O}^\bullet$ species contributes 3.1 % to the ground state wave function. Similarly, for complex **2** and **3**, the CAS(11,8) SCF calculations at equilibrium Co–O distance of 1.742 Å and 1.774 Å results in $\sigma_{(pz+dz^2)}^2 \pi_{(py+dyz)}^2 \pi_{(px+dxz)}^2 \pi_{(py+dyz)}^1 \square_{(dxy)}^2 \pi_{(px+dxz)}^2 \square_{(dx^2-y^2)}^0 \sigma_{(pz+dz^2)}^0$ and $\sigma_{(pz+dz^2)}^2 \pi_{(py+dyz)}^2 \pi_{(px+dxz)}^2 \pi_{(px+dxz)}^1 \pi_{(py+dyz)}^2 \square_{(dxy)}^2 \square_{(dx^2-y^2)}^0 \sigma_{(pz+dz^2)}^0$ configurations which corresponds to true $\text{Co}^{\text{IV}}=\text{O}$ species, contributing 70.3% and 64.2% to the total wave-function,

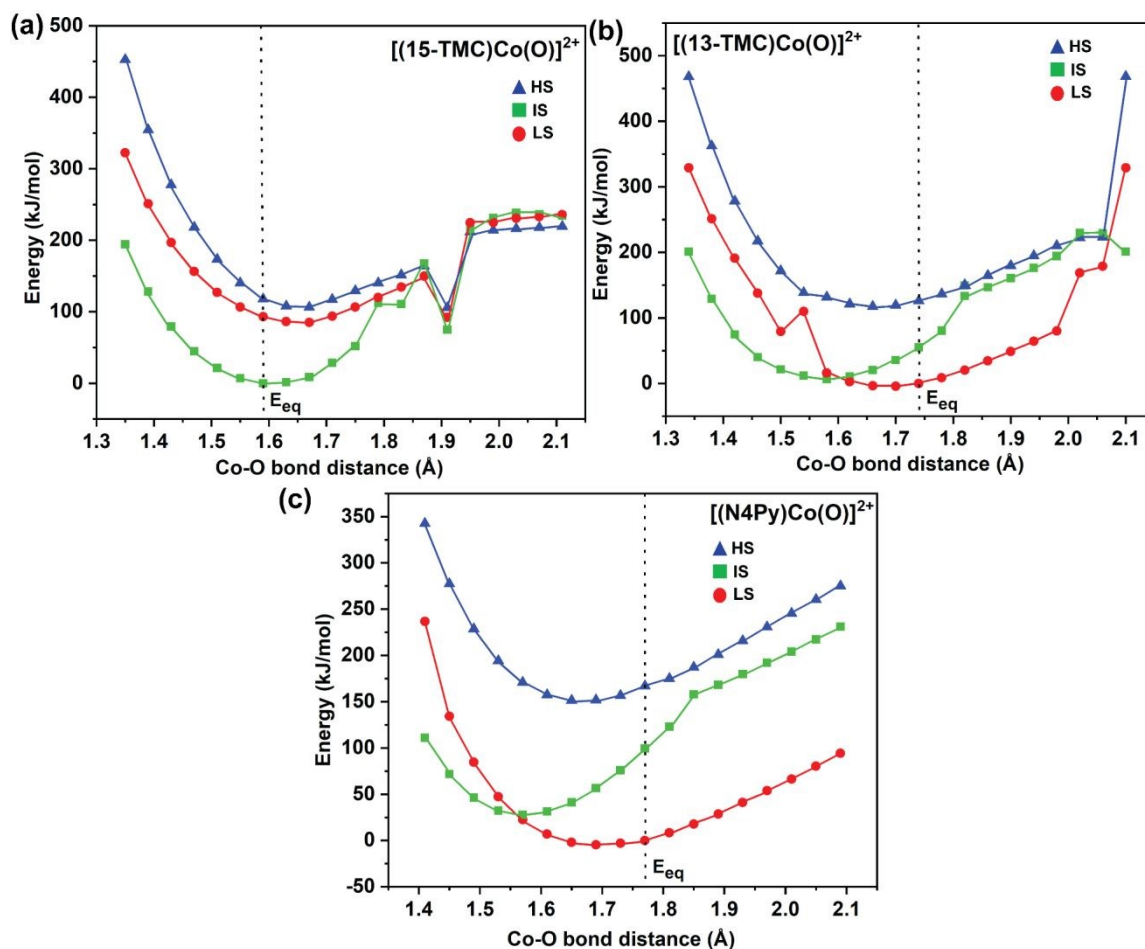


Figure 3: CASSCF/NEVPT2 estimated Potential energy surfaces scan of (a-c) **I-3** as a function of the Co–O distance.

respectively. Further, the following $\text{Co}^{\text{III}}-\text{O}^\bullet$ configuration $\sigma_{(pz+dz^2)}^2 \pi_{(py+dyz)}^2 \pi_{(px+dxz)}^1 \pi_{(py+dyz)}^1$
 $\square_{(dxy)}^2 \pi_{(px+dxz)}^2 \square_{(dx^2-y^2)}^0 \sigma_{(pz+dz^2)}^0$ and $\sigma_{(pz+dz^2)}^2 \pi_{(py+dyz)}^2 \pi_{(px+dxz)}^1 \pi_{(py+dyz)}^2 \square_{(dxy)}^2 \pi_{(px+dxz)}^2$
 $\square_{(dx^2-y^2)}^0 \sigma_{(pz+dz^2)}^0$ contributes 14.3%, and 20%, respectively to the ground state wave function.
 Thus, these results suggest that $\text{Co}^{\text{IV}}=\text{O}$ contribution is highest in species **1**, while $\text{Co}^{\text{III}}-\text{O}^\bullet$
 contribution is highest in species **3**. Furthermore, the calculation unequivocally suggest that in
 all three species both $\text{Co}^{\text{IV}}=\text{O}$ and $\text{Co}^{\text{III}}-\text{O}^\bullet$ species states are admixed at the ground state.

True $\text{Co}^{\text{IV}}=\text{O}$ vs $\text{Co}^{\text{III}}-\text{O}^\bullet$ Species: Role of spin-states

Further, to understand the role of Co–O bond length on dictating the stabilisation of two

View Article Online

DOI: 10.1039/D1FD00072A

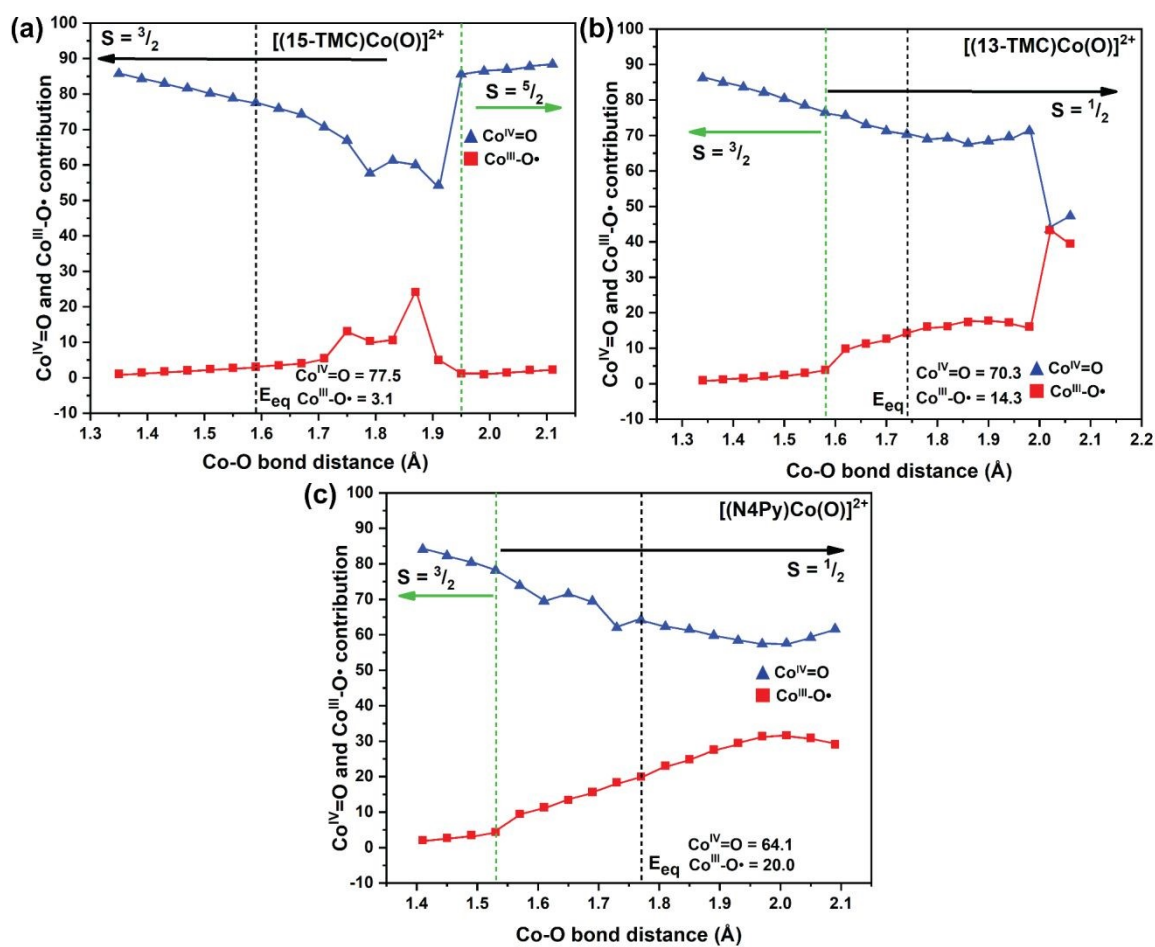


Figure 4: Per cent of the Co^{IV}=O and Co^{III}-O• species changes in (a-c) 1-3 as a function of the Co–O distance.

valance isomers, $\text{Co}^{\text{IV}}=\text{O}$ and $\text{Co}^{\text{III}}-\text{O}^{\bullet}$ species, we have performed a relaxed potential energy

[View Article Online](#)
DOI: 10.1039/D1FD00072A

surface scan along the Co–O bond coordinate for all three (**1-3**) species using DFT methods. All scan graphs consist of three segments, the minimum energy point, which corresponds to the equilibrium structure of the complex (optimised global minima), in both left and right sides of the graph with gradual decrease and increases in the Co–O bond distance, the energy of the system is found to be increasing steadily. The compression is, however, steeper, while elongation demands lesser energy strain (Figure 2). Using the ground state geometry obtained from the DFT calculations, we proceed further for CASSCF/NEVPT2 calculations on each scan point at an interval of 0.04 Å. Also, we have estimated vertical excitation energy of

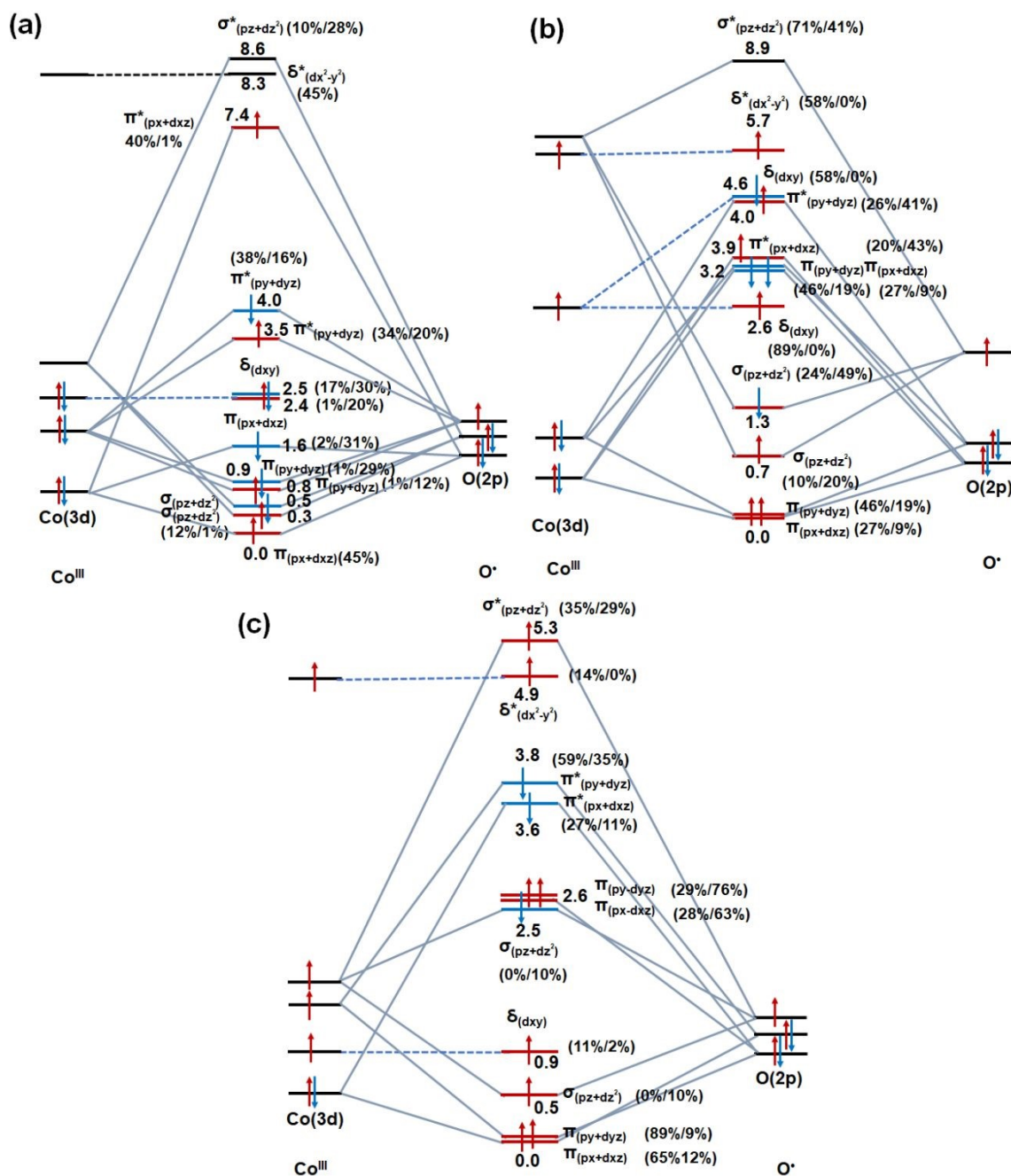


Figure 5: Molecular orbital diagram of Co=O unit (a) ls ($S = 1/2$), (b) is ($S = 3/2$) (c) hs ($S = 5/2$) spin-state in species **3**. The first value in the parenthesis is the % of p-character and the second value is the % of d-character in the particulate MO.

different spin states to understand the potential energy landscape. Figure 3 depicts the CASSCF/NEVPT2 calculated energy ordering of $S = 5/2$ (blue curve), $3/2$ (green curve) and $1/2$ (red curve) spin-states of species **1-3** along the Co–O bond coordinate. From the equilibrium point, as the Co–O bond-length elongates/compresses, the energy increases gradually for all spin states yielding a parabolic behaviour. For **1**, below the Co–O distance of 1.59 Å, the $S = 3/2$ state remains the ground state. However, elongation of the Co–O distance not only bring the excited states closer but also stabilise them as the high-spin ground state beyond the Co–O distance of 1.87 Å, suggests spin-crossover type behaviour for a very long bond length. The trend in the energetics of species **2** and **3** with respect to the Co–O bond distance is found to be similar. The ground state of $S = 1/2$ remains unaltered throughout the Co–O bond elongation for both **2** (except Co–O = 2.1 Å) and **3**. As we compress the Co–O bond, the energy gap among all three spin states decreases and at 1.58 Å (1.53 Å) distance for species **2** (**3**), $S = 3/2$ is stabilised as the ground state. Therefore, in **2** and **3**, the ground state of the $S = 1/2$ spin remains unaltered for the Co–O bond distance of $\sim 1.8 \pm 0.2$ Å, below/above which the $S = 3/2$ state becomes the ground state.

To understand the role of spin state and its correlation to the existence of $\text{Co}^{\text{IV}}=\text{O}$ vs $\text{Co}^{\text{III}}-\text{O}^\bullet$ species, the underlying configurations computed were analysed. Figure 4 depicts the changes in the contribution arising from the $\text{Co}^{\text{IV}}=\text{O}$ and $\text{Co}^{\text{III}}-\text{O}^\bullet$ character at various points. For species **1**, compression of Co–O distance from equilibrium point enhances the $\text{Co}^{\text{IV}}=\text{O}$ electromeric character reaching as high as $\sim 90\%$ at 1.35 Å; this is accompanied by a concomitant reduction in the $\text{Co}^{\text{III}}-\text{O}^\bullet$ character. Elongation of the Co–O bond from the equilibrium geometry enhances the $\text{Co}^{\text{III}}-\text{O}^\bullet$ character reaching $\sim 30\%$ at 1.87 Å with a concomitant reduction of $\text{Co}^{\text{IV}}=\text{O}$ species. Elongation of Co–O bond lengths beyond this point leads to enhancement of $\text{Co}^{\text{IV}}=\text{O}$ and reduction of $\text{Co}^{\text{III}}-\text{O}^\bullet$ species, though the nature of species at this long Co–O bond lengths are rather reflecting $\text{Co}^{\text{IV}}\cdots\text{O}^{2-}$ type species.

A similar trend is followed for species **2** and **3**. Compression of Co–O bond results in a steady decrease in the % of $\text{Co}^{\text{III}}-\text{O}^\bullet$ species and beyond 1.58 Å (species **2**) and 1.57 Å (species **3**), present in the form of $\text{Co}^{\text{IV}}=\text{O}$ species. As the Co-oxo bond distance decreases below these points, the ground state wave-function of these species are comprised of $> 75\%$ of the $\text{Co}^{\text{IV}}=\text{O}$ character with $< 4\%$ of oxyl-radical species. With the elongation, the $\text{Co}^{\text{III}}-\text{O}^\bullet$ character increases as high as $\sim 46\%$ for **2** and 31% for **3** at ~ 2.00 Å. Beyond Co–O distance of 2.00 Å, the contribution from $\text{Co}^{\text{IV}}=\text{O}$ species increases again.

To correlate the nature of $\text{Co}^{\text{IV}}=\text{O}$ vs $\text{Co}^{\text{III}}-\text{O}^\bullet$ species to the spin states, Figure 3 and Figure 4 need to be compared. The following points emerge with respect to species **1**: (i) as we compress the Co–O bond, the $\Delta(E_{3/2}-E_{1/2})$ gap decreases so does the $\text{Co}^{\text{III}}-\text{O}^\bullet$ character. This is accompanied by the concomitant increase of $\text{Co}^{\text{IV}}=\text{O}$ character. As the ground state remains $S = 3/2$ in these points with dominant $\text{Co}^{\text{IV}}=\text{O}$ species, indicating that $S = 3/2$ spin state favour $\text{Co}^{\text{IV}}=\text{O}$ species. (ii) As we elongate the Co–O bond, the $\Delta(E_{3/2}-E_{1/2})$ gap decreases and this is accompanied by an increase in $\text{Co}^{\text{III}}-\text{O}^\bullet$ radical character with a concomitant decrease of $\text{Co}^{\text{IV}}=\text{O}$ species. This is expected as the Co–O bond's elongation cleaves the corresponding π -bond leading to a favourable $\text{Co}^{\text{III}}-\text{O}^\bullet$ electrometer. At 1.87 Å, an $S = 1/2$ becomes the ground state, and coincidentally at this point, the $\text{Co}^{\text{III}}-\text{O}^\bullet$ character is the highest. This suggests that $S = 1/2$ favours $\text{Co}^{\text{III}}-\text{O}^\bullet$ species. (iii) Beyond Co–O distance of 1.95 Å, an $S = 5/2$ state becomes the ground state, and this is accompanied by a substantial increase of $\text{Co}^{\text{IV}}=\text{O}$ species, though a closer look at the electronic structure reveals a $\text{Co}^{\text{IV}}\cdots\text{O}^{2-}$ species due to relatively longer

bond lengths. While this does not affirm, $S = 5/2$ state with longer Co–O bond length seemingly favours $\text{Co}^{\text{IV}}=\text{O}$ species. For species **2** and **3**, the following points emerge (i) both have the ground state of $S = 1/2$ with compression of Co–O bond decreases the $\Delta(E_{1/2}-E_{3/2})$ gap increasing $\text{Co}^{\text{IV}}=\text{O}$ character and decreasing the $\text{Co}^{\text{III}}-\text{O}^\bullet$ character. Below ~ 1.55 Å, an $S = 3/2$ becomes the ground state, and this leads to a sharper increase in the $\text{Co}^{\text{IV}}=\text{O}$ character (see the change in slope in Figure 4b and c beyond the dotted green line). (ii) As we elongate the Co–O bond, an $S = 1/2$ stabilised in most of the points with a larger $\Delta(E_{1/2}-E_{3/2})$ gap, and this leads to a significant increase in the $\text{Co}^{\text{III}}-\text{O}^\bullet$ character. This is consistent with our assessment in species **1**.

To rationalise the spin-state dependency on the preference for $\text{Co}^{\text{IV}}=\text{O}$ vs $\text{Co}^{\text{III}}-\text{O}^\bullet$ species, a qualitative MO diagram based on DFT computed MOs and energies were plotted and shown in Figure 5a-c. Figure 5a shows the MO diagram for $\text{Co}^{\text{III}}-\text{O}^\bullet$ species with Co^{III} being in the low-spin state. Our calculations reveal that the degeneracy of all five metal d-orbitals and three oxo p-orbitals have lifted in the presence of ligand field with the bonding $\pi_{(\text{px}+\text{dxz})}$ orbital having a spin-up α -electron is the lowest in energy with 45% contribution from the oxygen p_x orbital followed by the $\sigma_{(\text{pz}+\text{dz}^2)}-\alpha > \sigma_{(\text{pz}+\text{dz}^2)}-\beta > \pi_{(\text{py}+\text{dyz})}-\alpha > \pi_{(\text{py}+\text{dyz})}-\beta > \pi_{(\text{py}+\text{dyz})}-\alpha > \pi_{(\text{py}+\text{dyz})}-\beta > \pi_{(\text{px}+\text{dxz})}-\beta$ lying at 0.3 eV, 0.5 eV, 0.8 eV, 0.9 eV and 1.6 eV, respectively. These bonding molecular orbitals are composed of contributions from the metal 3d- and oxygen 2p-orbitals. For instance, the bonding $\pi_{(\text{px}+\text{dxz})}$ MO with a spin-down β -electron consist of 31% d-character and merely 2% p-character from oxygen. The $\square_{(\text{dxy})}$ orbital is the non-bonding, containing a pair of electrons, lying at 2.4-2.5 eV. This non-bonding molecular orbital is followed by $\pi_{(\text{py}+\text{dyz})}-\alpha$ (3.5 eV) $>$ $\pi_{(\text{py}+\text{dyz})}-\beta$ (4.0 eV) $>$ $\pi_{(\text{px}+\text{dxz})}-\alpha$ (7.4 eV) $>$ $\square_{(\text{dx}^2-\text{y}^2)}$ (8.3 eV) $>$ $\sigma_{(\text{pz}+\text{dz}^2)}$ (8.4 eV). According to the energy ordering, the electrons are filling is as $[\pi_{(\text{px}+\text{dxz})}-\alpha]^1 > [\sigma_{(\text{pz}+\text{dz}^2)}-\alpha]^1 > [\sigma_{(\text{pz}+\text{dz}^2)}-\beta]^1 > [\pi_{(\text{py}+\text{dyz})}-\alpha]^1 > [\pi_{(\text{py}+\text{dyz})}-\beta]^1 > [\pi_{(\text{px}+\text{dxz})}-\beta]^1 > [\square_{(\text{dxy})}-\alpha]^1 > [\square_{(\text{dxy})}-\beta]^1 > [\pi_{(\text{py}+\text{dyz})}-\alpha]^1 > [\pi_{(\text{py}+\text{dyz})}-\beta]^1 > [\pi_{(\text{px}+\text{dxz})}-\alpha]^1 > [\square_{(\text{dx}^2-\text{y}^2)}] > [\sigma_{(\text{pz}+\text{dz}^2)}]$. From the orbital contribution values from metal 3d and oxygen 2p orbitals, it is noted that bonding and antibonding orbitals are heavily mixed with the contribution from metal and oxo centre. The singly occupied antibonding molecular orbital, $\pi_{(\text{px}+\text{dxz})}^*$, is found to be composed of 40% of p-character with a mere 1% of d-character, indicating the unpaired electron is located on an oxygen 2p orbital, reflecting a strong radical character as expected for the $\text{Co}^{\text{III}}-\text{O}^\bullet$ species. A qualitative bond order analysis, if performed, suggest that for this species, σ bond is $(\frac{2-0}{2} = 1)$ one and π bond is $0.5 (\frac{4-3}{2} = 0.5)$, suggesting an overall bond order of 1.5. For $\text{Co}^{\text{IV}}=\text{O}$ with $S = 3/2$ (intermediate spin state), the MO diagram (Figure 5b) reveal that the additional unpaired electron found in $\pi_{(\text{px}+\text{dxz})}^*$ orbital earlier is absent, and this electron in fact is present in non-

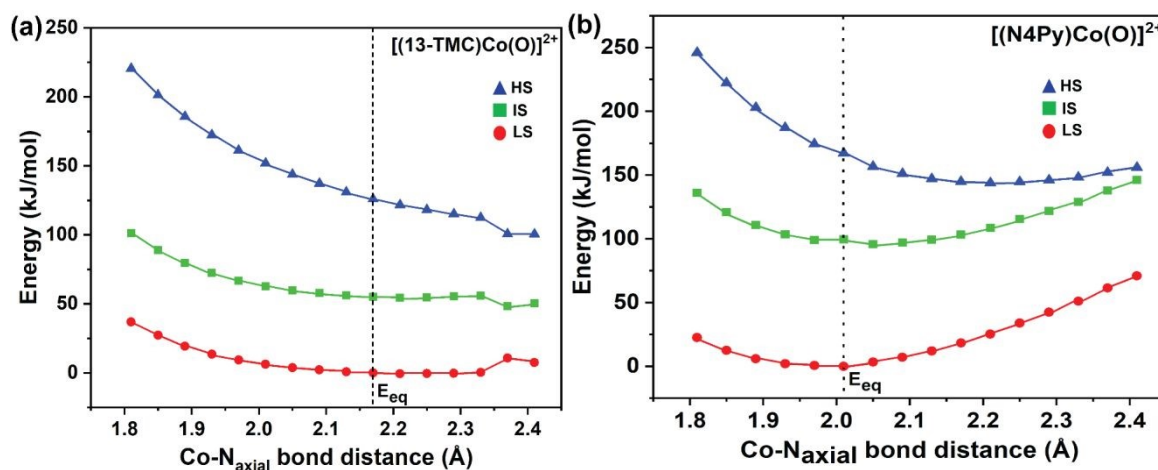


Figure 6: Potential energy surfaces of the lowest-energy states of (a-b) **I-2** as a function of the Co–N_{ax} distance.

bonding \square^* (dx^2-y^2) orbital. This enhances the π bond order, and here the bond order is as follows σ bond order is ($\frac{2-0}{2} = 1$) one and π bond is 1.0 ($\frac{4-2}{2} = 1$), suggesting an overall bond order of 2.0. For $\text{Co}^{\text{IV}}=\text{O}$ species with $S = 5/2$ spin state (high-spin) at the Co centre, the MO diagram (Figure 5c) reveals that the scenario is similar to the first case with the only change being that the σ^* (p_z+dz^2) orbital stabilises significantly due to very weak antibonding interactions. Due to these changes, the bond order is as follows: σ bond order is ($\frac{2-1}{2} = 0.5$) one and π bond is ($\frac{4-2}{2} = 1.0$), suggesting an overall bond order of 1.5.

Tool to Predict the per cent of $\text{Co}^{\text{III}}-\text{O}^\bullet$ vs $\text{Co}^{\text{IV}}=\text{O}$ species in Unknown Examples

After analysing the dependency of the $\text{Co}^{\text{IV}}=\text{O}/\text{Co}^{\text{III}}-\text{O}^\bullet$ equilibrium on the Co–O bond length, we have performed a potential energy surface scan along the Co– N_{ax} bond in **2** and **3**. As we have stated earlier, in complex **2**, a loosely bound CH_3CN molecule is attached in the apical position opposite to the Co-oxo unit. In contrast, the opposite apical position in **3** is occupied by one of the amine arms of the N4Py ligand. Figure 6 shows the variation in energy in different spin states as a function of Co– N_{ax} bond-length where spin-state splittings and the nature of the ground state are unaltered. For both **2** and **3**, as we elongate the Co– N_{ax} distance, the energy of individual spin states initially decreases and then increases slowly (Figure 6). Further, CAS(11,8) calculations on the stationary points in an interval of the 0.04 Å on the Co– N_{ax} scan surface reveal that in complex **2**, with the decrease in the Co– N_{ax} bond distance, the oxyl radical character increases and reaches 20.2% at Co– N_{ax} distance of 1.81 Å and vice versa. In **3**, a similar trend is followed, but the extent of the rise of oxyl radical character with lowering the Co– N_{ax} bond distance is comparatively significant. Therefore, the existence of $\text{Co}^{\text{III}}-\text{O}^\bullet$ isomer is directly dependent on the Co–O as well as Co– N_{ax} bond-lengths. Previous reports show that the $\text{M}=\text{O}$ antibonding interactions were found to push the ligand d_z^2 orbital present in the axial position to the $\text{M}=\text{O}$ moiety and result in $\text{M}-L_{\text{ax}}$ bond elongation; this push-pull effect is known to influence the reactivity of $\text{Fe}^{\text{IV}}=\text{O}$ species.^{40, 41} Considering these points, we attempt to develop a tool based on the structural parameter to estimate approximately the % of $\text{Co}^{\text{III}}-\text{O}^\bullet$ species for any high-valent (+III/+IV) Co-oxo complexes looking at the ratio of Co–O/Co– N_{ax} as shown below,

$$\% \text{Co}^{\text{III}}-\text{O}^\bullet \propto \frac{d_{(\text{Co}-\text{O})}}{d_{(\text{Co}-N_{\text{ax}})}}$$

Our calculations reveal that the higher the $\frac{d_{(\text{Co}-\text{O})}}{d_{(\text{Co}-N_{\text{ax}})}}$ ratio (termed as R_d), greater will be the $\text{Co}^{\text{III}}-\text{O}^\bullet$ contribution. This relationship shown above yields a linear correlation as shown in Figure 7 for both **2** and **3** with varying slopes. We fit the points for a linear equation (Figure 7), which yield a very good fit (R^2 value exceeding 0.98). Using the parameters derived, one can calculate the % of $\text{Co}^{\text{III}}-\text{O}^\bullet$ species for any given complex. As DFT calculations often yield this structural information, the electromeric ratio for an unknown species can be calculated directly.

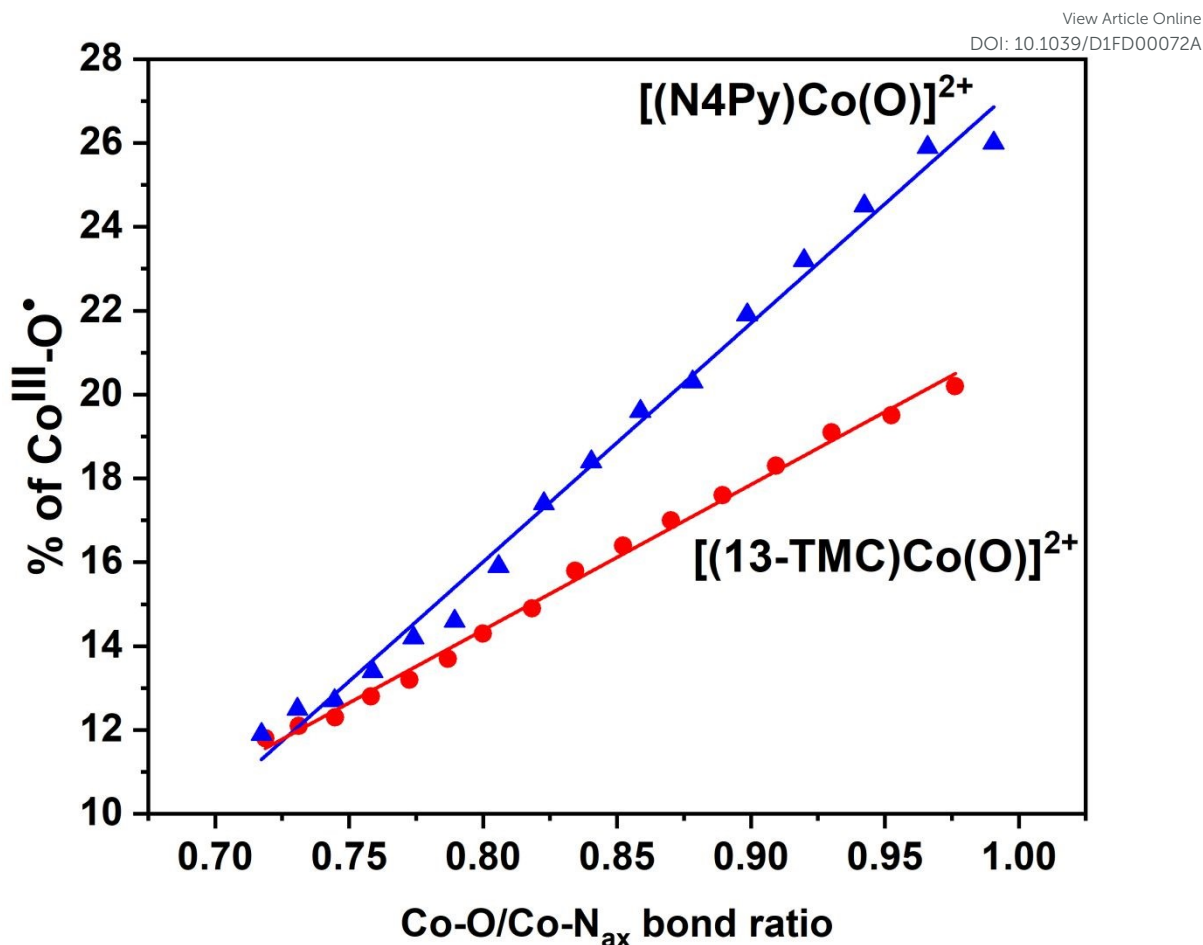


Figure 7: % of the Co^{III}-O• isomer in **2** and **3** as a function of the Co-N_{ax} distance. Red and blue points are for [(13-TMC)Co(O)(CH₃CN)]²⁺ and [(N4Py)Co(O)]²⁺ complexes respectively. The linear fit has performed using $y = mx + C$ equation, where the slopes are 34.69 ± 0.63 and 56.94 ± 1.38 respectively. The intercept values are -13.37 ± 0.53 and -29.55 ± 1.17 for the respective red and blue graph. For both cases, R-square values are greater than 0.99.

Co^{III}-O• vs CO^{IV}=O species in five-coordinate square-pyramidal geometry?

When the axial CH₃CN ligand in [(13-TMC)Co^{IV}(O)(CH₃CN)]²⁺ elongates to an infinite distance, it will result in the formation of a square pyramidal [(13-TMC)Co^{IV}(O)]²⁺ complex.¹⁹ This metastable monomeric non-heme complex is photocatalytically synthesised and characterised by Nam and co-workers. Various spectroscopic studies have been performed to establish the presence of the Co^{IV}=O core in this molecule. DFT calculations on this molecule show that the molecule possesses an intermediate $S = 3/2$ state as the ground state, with the low-spin and high-spin states are lying at 15.2 kJ/mol and 46.0 kJ/mol higher in energy. The ground state of $S = 3/2$ remains unchanged in the CASSCF/NEVPT2 calculations. A quartet ground state agrees with the experimental observation. The Co-O and Co-N_{eq} bonding parameters in the ground $S = 3/2$ state are 1.684 Å, 2.036 Å, 2.057 Å, 2.041 Å, 2.127 Å (Figure 8). A CAS (11,8) calculation on this molecule predicts that the presence of 69% of Co^{IV}=O character along

with a small % of $\text{Co}^{\text{III}}\text{-O}^\bullet$ character (7.0 %) in the ground state. The ground state wavefunction is dominated by the $\sigma_{(\text{pz}+\text{dz}^2)}^2 \pi_{(\text{px}+\text{dxz})}^2 \pi_{(\text{py}+\text{dyz})}^2 \square_{(\text{dxy})}^2 \pi_{(\text{px}+\text{dxz})}^1 \pi_{(\text{py}+\text{dyz})}^1 \square_{(\text{dx}^2-\text{y}^2)}^1 \sigma_{(\text{pz}+\text{dz}^2)}^0$ configuration (55.3%) while the contribution of $\sigma_{(\text{pz}+\text{dz}^2)}^1 \pi_{(\text{px}+\text{dxz})}^2 \pi_{(\text{py}+\text{dyz})}^2 \square_{(\text{dxy})}^2 \pi_{(\text{py}+\text{dyz})}^1 \pi_{(\text{px}+\text{dxz})}^1 \square_{(\text{dx}^2-\text{y}^2)}^1 \sigma_{(\text{pz}+\text{dz}^2)}^1$ and $\sigma_{(\text{pz}+\text{dz}^2)}^1 \pi_{(\text{px}+\text{dxz})}^2 \pi_{(\text{py}+\text{dyz})}^2 \square_{(\text{dxy})}^2 \pi_{(\text{py}+\text{dyz})}^1 \pi_{(\text{px}+\text{dxz})}^1 \square_{(\text{dx}^2-\text{y}^2)}^1 \sigma_{(\text{pz}+\text{dz}^2)}^1$ configuration is less, 13.2 % and 7.0% respectively, indicating the presence of $\text{Co}^{\text{IV}}=\text{O}$ character in this complex.

From the earlier detailed analysis and MO diagram presented, it is clear that the dominant $\text{Co}^{\text{IV}}=\text{O}$ character present in this complex is due to stabilisation of $S = 3/2$ ground state. Further to assess the linear correlation estimated, we have taken the computed Co-O distance of 1.684 Å and approximated the non-existent axial ligand to 3.0 Å. This yield % $\text{Co}^{\text{III}}\text{-O}^\bullet$ character as 6.1 and this is similar to 7.0 % obtained from the CASSCF calculations. This suggests the portability of this relationship even to a square pyramidal geometry, offering confidence on the proposed tool to calculate the $\text{Co}^{\text{III}}\text{-O}^\bullet$ radical character.

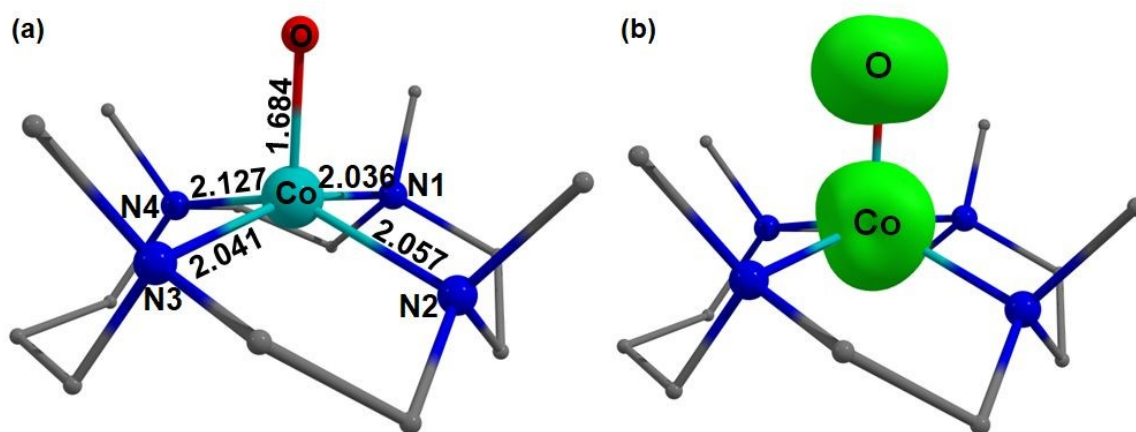


Figure 8: (a) B3LYP-D3 optimised structure and (b) spin density plot of the ground state of complex 4.

Valance Electromerism Before the oxo wall?

To compare and contrast the $\text{M}=\text{O}$ vs $\text{M}-\text{O}^\bullet$ species before the oxowall, we have extended our calculations to Mn and Fe-analogues of $[(\text{N4Py})\text{Co}(\text{O})]^{2+}$ species.^{3 42} For both $[(\text{N4Py})\text{Fe}(\text{O})]^{2+}$ (**5**) and $[(\text{N4Py})\text{Mn}(\text{O})]^{2+}$ (**6**) species an $S = 3/2$ and $S = 1$ spin state is found to be the ground state⁴³ and this is in agreement with the experiments and previous DFT calculations. The other spin states lying higher in energy (103.2 kJ/mol, 126.4 kJ/mol for $S = 2$ and $S = 0$ states in $[(\text{N4Py})\text{Fe}(\text{O})]^{2+}$, respectively and 38.2 kJ/mol for the $S = 1/2$ spin in $[(\text{N4Py})\text{Mn}(\text{O})]^{2+}$). Here also, DFT calculations show a overdelocalisation problem, where the spin density values on the metal (Fe/Mn) and on the oxyl moiety, are 1.244 and 0.828; 2.510 and 0.599 respectively (Figure 9). The CAS(10,8)/NEVPT2 and CAS(9,8)/NEVPT2 calculations reveal that the energy ordering of spin states are unaltered. For $[(\text{N4Py})\text{Mn}(\text{O})]^{2+}$ species a CAS calculation unveils a 74.6% contribution from the $\sigma_{(\text{pz}+\text{dz}^2)}^2 \pi_{(\text{py}+\text{dyz})}^2 \pi_{(\text{px}+\text{dxz})}^2 \square_{(\text{dxy})}^1 \pi_{(\text{py}+\text{dyz})}^1 \pi_{(\text{px}+\text{dxz})}^1 \square_{(\text{dx}^2-\text{y}^2)}^0 \sigma_{(\text{pz}+\text{dz}^2)}^0$ configuration corresponding to $\text{Mn}^{\text{IV}}=\text{O}$ species with a little (~8%) contribution from $\sigma_{(\text{pz}+\text{dz}^2)}^1 \pi_{(\text{py}+\text{dyz})}^2 \pi_{(\text{px}+\text{dxz})}^2 \square_{(\text{dxy})}^1 \pi_{(\text{py}+\text{dyz})}^1 \pi_{(\text{px}+\text{dxz})}^1 \square_{(\text{dx}^2-\text{y}^2)}^0 \sigma_{(\text{pz}+\text{dz}^2)}^1$

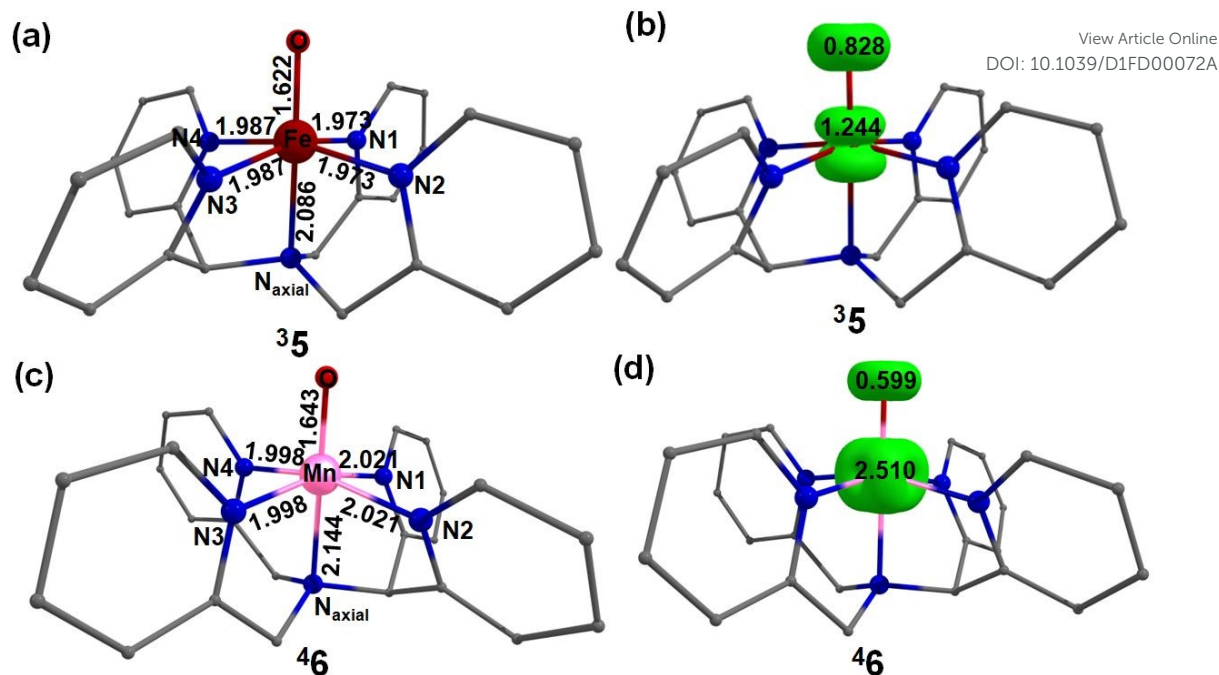
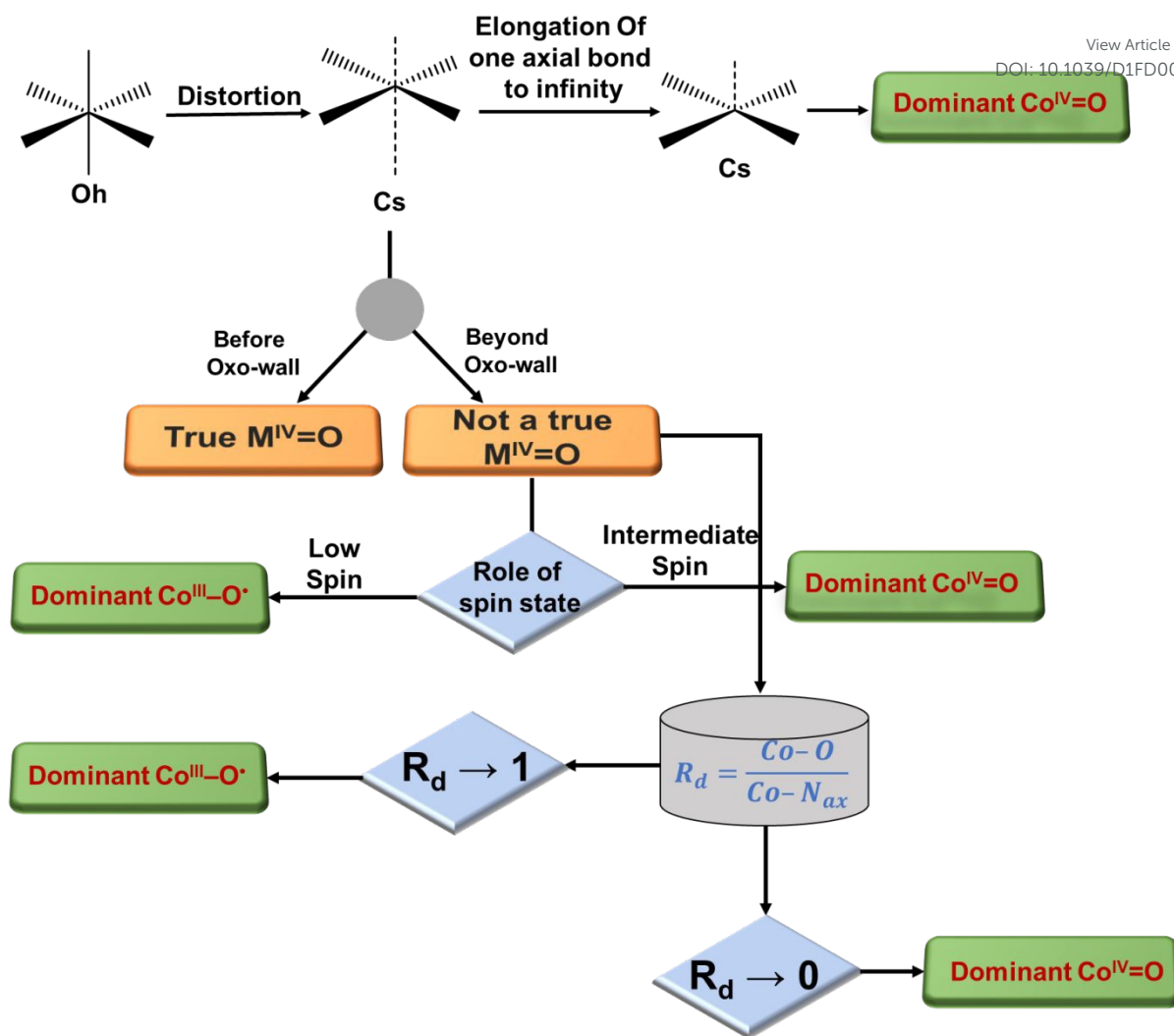


Figure 9: (a,c) B3LYP-D3 optimised structure and (b,d) spin density plots of the ground state of complexes 5-6.

configuration that corresponds to the $\text{Mn}^{\text{III}}\text{-O}^{\bullet}$ species. Similarly, the ground state wave function of $[(\text{N4Py})\text{Fe}(\text{O})]^{2+}$ species consist of 73% of $\sigma_{(\text{pz}+\text{dz}^2)}^2 \pi_{(\text{py}+\text{dyz})}^2 \pi_{(\text{px}+\text{dxz})}^2 \square_{(\text{dxy})}^2 \pi_{(\text{px}+\text{dxz})}^1 \pi_{(\text{py}+\text{dyz})}^1 \square_{(\text{dx}^2-\text{y}^2)}^* \sigma_{(\text{pz}+\text{dz}^2)}^0$ configuration ($\text{Fe}^{\text{IV}}=\text{O}$) and $\sim 5\%$ of $\sigma_{(\text{pz}+\text{dz}^2)}^1 \pi_{(\text{py}+\text{dyz})}^2 \pi_{(\text{px}+\text{dxz})}^2 \square_{(\text{dxy})}^2 \pi_{(\text{px}+\text{dxz})}^1 \pi_{(\text{py}+\text{dyz})}^1 \square_{(\text{dx}^2-\text{y}^2)}^* \sigma_{(\text{pz}+\text{dz}^2)}^1$ configuration ($\text{Fe}^{\text{III}}\text{-O}^{\bullet}$). This reveals that before group 8, the complexes are stable with the $\text{M}=\text{O}$ formalism with a very small/insignificant contribution from their oxyl-radical counterpart.

Take home message

In the present work, we have employed the density function theory (DFT) and *ab initio* method to study one of the outstanding problems in biomimic chemistry that have existed for a very long time, .i.e the existence of double bond character beyond the group 8 molecule. The originally proposed oxo-wall theory is strictly applicable to tetragonal complexes, and for other geometries or coordination numbers, oxo-wall does not strictly forbid the formation of ideal $\text{M}^{\text{IV}}=\text{O}$ species. Over the last few years, several synthetic groups employed different ligand architecture to synthesise a true $\text{Co}^{\text{IV}}=\text{O}$ species. Although this would not violate the oxo-wall theory proposed by B&G, the possibility that the $\text{Co}^{\text{IV}}=\text{O}$ species could exist along with its electromer $\text{Co}^{\text{III}}\text{-O}^{\bullet}$ has not been explored and has been the subject of this study. We arrived at the following take-home messages by thoroughly studying six different metal-oxo species (see Scheme 2).



Scheme 2: Take home message of the work presented here.

(i) Prior to the wall (before group 8), the high-valent (+4) terminal M-Oxo species exist in their formal $M^{IV}=O$ form. The ground state wave-function is composed of $\sim 80\%$ of $M^{IV}=O$ character with very small/negligible $M^{III}-O^{\bullet}$ character.

(ii) After the oxo-wall (beyond group 8), our calculations reveal a drastic decrease of formal $Co^{IV}=O$ character accompanied by a concomitant increase of isomeric $Co^{III}-O^{\bullet}$ species. This suggests that irrespective of the geometry, obtaining a true $Co^{IV}=O$ species (100% $Co^{IV}=O$ character and 0% $Co^{III}-O^{\bullet}$) is hard.

(iii) Secondly, we look at the dominant character of $Co^{IV}=O$ vs $Co^{III}-O^{\bullet}$ under various conditions. Our calculations reveal that a formal $Co^{IV}=O$ species is dominant if an $S = 3/2$ spin state is the ground state and isomeric $Co^{III}-O^{\bullet}$ species composition is substantial if $S = 1/2$ low-spin state is the ground state.

(iv) By analysing thoroughly various parameters, we propose that $\% Co^{III}-O^{\bullet} \propto \frac{d_{(Co-O)}}{d_{(Co-N_{ax})}}$ ($d_{(Co-O)}$ and $d_{(Co-N_{ax})}$ are distances of axial $Co-O$ and $Co-N_{ax}$ bonds in Å), and this

relationship yields a linear correlation for two different Co complexes studied, offering a chance to directly calculate the % of Co^{III}-O• character in any unknown system. Our calculations suggest that the larger the bond ratio, the higher will be the Co^{III}-O• character with values closer to zero yielding an ideal Co^{IV}=O species. Surprisingly the proposed correlation is portable even to square pyramidal geometry to assess the per cent of Co^{III}-O• character.

Acknowledgement

We thank DST and SERB (CRG/2018/00430; DST/CSA-03/2018-10; SB/SJF/2019-20/12) for funding.

References:

1. D. G. Nocera, *Acc. Chem. Res.*, 2012, **45**, 767-776.
2. M. Wikström, K. Krab and V. Sharma, *Chem. Rev.*, 2018, **118**, 2469-2490.
3. M. Costas, M. P. Mehn, M. P. Jensen and L. Que, *Chem. Rev.*, 2004, **104**, 939-986.
4. C. Krebs, D. Galonic Fujimori, C. T. Walsh and J. M. Bollinger Jr, *Acc. Chem. Res.*, 2007, **40**, 484-492.
5. W. Nam, *Journal*, 2007.
6. A. Borovik, *Chem. Soc. Rev.*, 2011, **40**, 1870-1874.
7. R. Kumar, B. Pandey, A. Sen, M. Ansari, S. Sharma and G. Rajaraman, *Coordination Chemistry Reviews*, 2020, **419**, 213397.
8. A. Sen, N. Vyas, B. Pandey and G. Rajaraman, *Dalton Trans.*, 2020, **49**, 10380-10393.
9. S. Rana, J. P. Biswas, A. Sen, M. Clémancey, G. Blondin, J.-M. Latour, G. Rajaraman and D. Maiti, *Chem. Sci.*, 2018, **9**, 7843-7858.
10. A. Gunay and K. H. Theopold, *Chem. Rev.*, 2010, **110**, 1060-1081.
11. H. B. Gray and J. R. Winkler, *Acc. Chem. Res.*, 2018, **51**, 1850-1857.
12. H. B. Gray, *Chem. Int.*, 2019, **41**, 16-19.
13. V. A. Larson, B. Battistella, K. Ray, N. Lehnert and W. Nam, *Nature Reviews Chemistry*, 2020, **4**, 404-419.
14. C. J. Ballhausen and H. B. Gray, *Inorg. Chem.*, 1962, **1**, 111-122.
15. H. B. Gray and C. R. Hare, *Inorg. Chem.*, 1962, **1**, 363-368.
16. J. R. Winkler and H. B. Gray, *Molecular Electronic Structures of Transition Metal Complexes I*, 2011, 17-28.
17. S. Ye and F. Neese, *Proc. Natl. Acad. Sci. U.S.A.*, 2011, **108**, 1228-1233.
18. K.-B. Cho, S. Shaik and W. Nam, *J. Phys. Chem. Lett.*, 2012, **3**, 2851-2856.
19. B. Wang, Y.-M. Lee, W.-Y. Tcho, S. Tussupbayev, S.-T. Kim, Y. Kim, M. S. Seo, K.-B. Cho, Y. Dede and B. C. Keegan, *Nat. Commun.*, 2017, **8**, 1-10.
20. H. Kurreck, B. Kirste and W. Lubitz, *Angew. Chem. Int. Ed.*, 1984, **23**, 173-194.
21. M. Frisch, G. Trucks, H. Schlegel, G. Scuseria, M. Robb, J. Cheeseman, G. Scalmani, V. Barone, G. Petersson and H. Nakatsuji, *Journal*, 2016.
22. R. H. Hertwig and W. Koch, *Chem. Phys. Lett.*, 1997, **268**, 345-351.
23. F. A. Hamprecht, A. J. Cohen, D. J. Tozer and N. C. Handy, *J. Chem. Phys.*, 1998, **109**, 6264-6271.
24. L. E. Roy, P. J. Hay and R. L. Martin, *J. Chem. Theory Comput.*, 2008, **4**, 1029-1031.
25. V. A. Rassolov, J. A. Pople, M. A. Ratner and T. L. Windus, *J. Chem. Phys.*, 1998, **109**, 1223-1229.
26. A. V. Marenich, C. J. Cramer and D. G. Truhlar, *J. Phys. Chem. B*, 2009, **113**, 6378-6396.
27. F. Neese, *Wiley Interdisciplinary Reviews: Computational Molecular Science*, 2018, **8**, e1327.
28. M. Reiher, *Theoretical Chemistry Accounts*, 2006, **116**, 241-252.

29. G. Zhurko and D. Zhurko, URL: <http://www.chemcraftprog.com>, 2009.
30. D. Kim, J. Cho, Y.-M. Lee, R. Sarangi and W. Nam, *Chemistry (Weinheim an der Bergstrasse, Germany)*, 2013, **19**, 14112. Online
DOI: 10.1039/D1FD00072A
31. W. K. Lo, C. E. Castillo, R. Gueret, J. Fortage, M. Rebarz, M. Sliwa, F. Thomas, C. J. McAdam, G. B. Jameson and D. A. McMorrnan, *Inorg. Chem.*, 2016, **55**, 4564-4581.
32. M. Zhang, M. De Respinis and H. Frei, *Nat. Chem.*, 2014, **6**, 362-367.
33. M. Atanasov, P. Comba, B. Martin, V. Müller, G. Rajaraman, H. Rohwer and S. Wunderlich, *J. Comput. Chem.*, 2006, **27**, 1263-1277.
34. T. Z. Gani and H. J. Kulik, *J. Chem. Theory Comput.*, 2016, **12**, 5931-5945.
35. E. R. Johnson, A. Otero-De-La-Roza and S. G. Dale, *J. Chem. Phys.*, 2013, **139**, 184116.
36. R. Gupta, T. Taguchi, B. Lassalle-Kaiser, E. L. Bominaar, J. Yano, M. P. Hendrich and A. Borovik, *Proc. Natl. Acad. Sci. U.S.A.*, 2015, **112**, 5319-5324.
37. H. Chen, W. Lai and S. Shaik, *J. Phys. Chem. Lett.*, 2010, **1**, 1533-1540.
38. P. E. Siegbahn, J. Almlöf, A. Heiberg and B. O. Roos, *J. Chem. Phys.*, 1981, **74**, 2384-2396.
39. J. Olsen, *Int. J. Quantum Chem.*, 2011, **111**, 3267-3272.
40. Z. Ma, N. Nakatani, H. Fujii and M. Hada, *Phys. Chem. Chem. Phys.*, 2020, **22**, 12173-12179.
41. R. Wang and S. P. de Visser, *Journal of inorganic biochemistry*, 2007, **101**, 1464-1472.
42. D. F. Leto, R. Ingram, V. W. Day and T. A. Jackson, *Chemical Communications*, 2013, **49**, 5378-5380.
43. D. Kumar, H. Hirao, L. Que and S. Shaik, *J. Am. Chem. Soc.*, 2005, **127**, 8026-8027.